Assimilating WIVERN windpseudo-observations in WRF model: an application to the outstanding case of the Medicane Ianos

Journal of Energy Storage 161 (2026) 121868

Contents lists available at ScienceDirect

Journal of Energy Storage

journal homepage: www.elsevier.com/locate/est

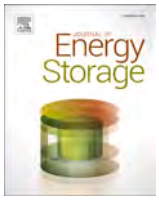

Research papers

Pore scale applications of Phase-field Lattice Boltzmann Methods for underground CH_4, H_2 and CO_2 storage

Alice Raeli [a,*], Eloisa Salina Borello [a], Cristina Serazio [a], Luiz Eduardo Czelusniak [b], Tim Niklas Bingert [b], Mathias J. Krause [b], Dario Viberti [a]

[a] Politecnico di Torino, DIATI Dipartimento di Ingegneria dell'Ambiente, del Territorio e delle Infrastrutture, Corso Duca degli Abruzzi, 24, 10129, Torino, Italy
[b] KIT Karlsruhe Institute of Technology, Kaiserstraße 12, 76131 Karlsruhe

ARTICLE INFO

Keywords:
Lattice Boltzmann method
OpenLB
Multiphase fluid flow
Pore-scale characterization
Underground storage
HPC simulation

ABSTRACT

The design of sustainable large-scale underground energy storage systems relies on accurate reservoir dynamic modelling. Key macroscopic parameters, such as critical saturations, capillary pressure, and relative permeabilities, are strongly influenced by pore-scale multiphase flow phenomena and trapping mechanisms. The analysis of multiphase flow behavior at the pore scale can therefore improve reservoir characterization and support engineering applications, including underground storage of natural gas (UGS), hydrogen (UHS), and carbon dioxide.

This study investigates numerical modelling of imbibition and drainage processes, representative of withdrawal and injection scenarios, using the Lattice Boltzmann Method (LBM). Owing to its inherent parallel structure and flexibility in handling complex geometries, LBM provides an efficient framework for simulating multiphase flow in porous media. However, previous studies have often applied LBM to simplified porous geometries or relied on boundary conditions that were not designed to handle phase transitions at the outflow boundary in evolving multiphase systems.

In this work, the open-source parallel library OpenLB is tailored and adapted to simulate two-phase flows governed by the Allen–Cahn equation in two-dimensional porous domains. The proposed developments overcome previous limitations by enabling the simulation of more realistic geometries and by implementing outflow boundary conditions that allow phase interfaces to dynamically cross the outlet.

The simulated domains were designed to reproduce physical 2D micromodels (Rock-on-a-Chip) representative of reservoir rocks, focusing on H_2, CH_4, and CO_2–brine systems, with brine representing formation water. After validation against laboratory experiments, the numerical framework is intended to extend the analysis to reservoir conditions that are difficult to reproduce experimentally.

1. Introduction

The investigation of multiphase flow phenomena at the pore scale [1,2] is fundamental in several applications of geo-energy engineering and environmental science [3]. Important examples are underground storage of natural gas (UGS), hydrogen (UHS), and carbon dioxide in which the definition of the reservoir management strategy requires a thorough analysis and understanding of fluid flow phenomena, particularly when a non-native fluid is injected in a fully saturated geological formation (e.g., hydrogen and carbon dioxide in saline aquifers and/or depleted gas reservoirs). Several crucial parameters adopted in full-field reservoir modelling, such as residual and critical saturations, capillary forces, and relative permeabilities, are strongly related to the fluid's dynamic behavior at the pore scale [4–7]. It follows that their proper characterization and understanding have a significant impact on defining an optimized management strategy for underground energy storage systems.

This work aims to simulate two-phase imbibition and drainage processes in 2D synthetic physical micromodels designed to be representative of real or realistic pore structures [8,9]. The focus is placed on 2D micromodels because our purpose is to validate the simulations against experimental results obtained under laboratory conditions, in order to provide reliable numerical simulations under reservoir conditions,

* Corresponding author.
E-mail addresses: alice.raeli@polito.it (A. Raeli), eloisa.salinaborello@polito.it (E. Salina Borello), cristina.serazio@polito.it (C. Serazio), luiz.czelusniak@partner.kit.edu (L.E. Czelusniak), tim.bingert@kit.edu (T.N. Bingert), mathias.krause@kit.edu (M.J. Krause), dario.viberti@polito.it (D. Viberti).

https://doi.org/10.1016/j.est.2026.121868
Received 13 November 2025; Received in revised form 27 February 2026; Accepted 27 March 2026
Available online 3 April 2026

Nomenclature

dx	Space step
dt	Time step
ν	Kinematic viscosity
u, u_m, u^*	Velocity / mean / Darcy
ρ	Density
σ	Interfacial tension
κ	Permeability
μ_{inj}	Dynamic viscosity injected fluid
μ_r	Dynamic viscosity resident fluid
p	Pressure
p_c	Capillary Pressure
S_w	Water saturation
θ	Contact angle
ϕ	Phase order parameter

which are difficult to reproduce experimentally. The final target is the characterization of displacement regimes and phenomena (trapping mechanism, viscous and capillary fingering) for a given set of pore geometries and different fluid combinations. This study examines how differences in the composition of the injected fluid (pure CO_2, CH_4, and H_2) influence the equilibrium between capillary and viscous forces, and hence the resulting flow behavior.

The lattice Boltzmann method (LBM) has emerged as a powerful alternative to traditional Computational Fluid Dynamics (CFD) techniques, such as Finite Volume Method (FVM), which is used here for comparison. Its popularity derives from its computational efficiency, straightforward implementation, and natural suitability for massively parallel architectures such as GPUs [10–13]. LBM has been extensively applied to pore scale simulation [14–17], allowing the direct simulation of drainage and imbibition processes on geometries reconstructed from micro-CT or generated synthetically. Early studies, such as [18], established the potential of LBM for simulating multiphase displacement in digitized sandstone. Colour-gradient approach and its recent developments were applied to porous media micro-CT simulation [17,19,20], EOR optimization [21], and three-phases simulation for CO_2 enhanced oil recovery and storage [21]. [22] proposed a coupled pseudopotential plus colour-gradient LBM to simulate three-phase immiscible flow with phase change and applied it to porous media displacement problems. In [23] phase-field LBM was validated against 2D micromodel experiments for the investigation of CO_2 sequestration at the pore scale, while [24,25] examined capillary effects at the outlet boundary in LBM application and proposed a phase-field local hybrid Allen-Cahn model with constant pressure inlet boundary conditions distributed in several injection holes. Recently, [26] adopted a phase-field approach to model multiphase flow in presence of large density ratios, whereas [27] applied the phase-field method to simulate multiphase flow in a 3D rough fracture.

Despite the significant advances achieved by these studies, several limitations can still be identified. All the cited approaches employ porous media with porosity values typically above 0.3, which do not fully represent the low-porosity and irregular morphologies often found in natural reservoir rocks, where complex pore connectivity and narrow throats strongly influence multiphase flow dynamics. The tested geometries are characterized by round-shaped grains, often homogeneous and regularly packed, limiting the representativeness of the pore-scale micromodels. Moreover, most published investigations focus on either drainage or imbibition separately and/or do not explicitly address the post-outflow regime, resulting in incomplete descriptions of phase redistribution once the displacement front reaches the outlet. Furthermore, viscosity and density ratios remain constrained to moderate ranges, far from those encountered in realistic reservoir conditions. Comprehensive open-source implementations that are optimized for realistic rock morphologies, parallelized for high-performance computing (HPC) architectures, and validated against experimental micromodels remain uncommon, due to challenges related to interface stability, computational scalability, and the physical parameterization required for reservoir-relevant conditions.

In the current research, pseudo-real rock 2D micromodels were considered. Two micromodels were generated by manipulating sections of *Micro Computed Tomography* (Micro-CT) images available in literature [7,28–32], thus yielding realistic irregular porous patterns. In addition, a 2D domain was obtained using Voronoi tessellation [33–35] to produce very thin channels and, consequently, very low porosity and permeability, mimicking conditions typical of geological formations relevant for energy storage. The permeability of each micromodel was evaluated through single-phase simulations, in which water was used as both saturating and injected fluid.

Monophase LBM solver results were compared at different resolutions and with the proposed multiphase approach, considering the injected and the resident fluid as the same fluid, for validation purposes. A comparison with permeability values obtained using the OpenFOAM CFD solver was also provided.

For each geometry, both drainage and imbibition scenarios were simulated under reservoir conditions, where brine was the wetting fluid and gas (either CO_2, CH_4, or H_2) was the non-wetting fluid. The fluid was injected by controlling the pressure gradient, simulating pressure-driven flows; the current setup can cover a broad spectrum of flow scenarios [25,36]. The simulations covered the entire displacing process, including the outflow of the injected fluid. For one of the imbibition scenarios, a comparison with OpenFOAM results was also provided.

A parallel and efficient open source LBM implementation was used: the latest release of the open-source OpenLB library [37,38]. Among its various applications in CFD problems, this library can handle very large-scale fluid flow simulations in porous media with complex geometries. Previous release of the code have mainly included three multi-phase LBM approaches: the Shan-Chen model, the Cahn-Hilliard free-energy model [13,24,39–43], and the Allen-Cahn phase-field model [24,41,44–48]. The Allen-Cahn model was chosen in this work for its numerical stability when handling large density ratios between fluids [26,47,49,50]. However, several modifications were required to adapt the methodology to the considered scenarios, which involve several numerical challenges such as irregular patterns, numerous corners, and high density and viscosity ratios between fluids. In particular, the pressure boundary conditions for the multiphase flow were optimized to mitigate numerical instabilities occurring when the outgoing fluid changes; furthermore, the Smagorinsky constant, which introduces adaptive diffusion in regions with strong gradients, was tuned to stabilize the numerical solution efficiently under the demanding conditions of the considered scenarios.

The current OpenLB release includes an example of a multiphase porous media application based on the optimized phase-field solver developed according to the analysis presented in this work; the example is provided as a ready-to-run case starting from a VTI file. Additional optimizations are currently in development.

Micro-scale porous media analysis requires fine spatial resolution to accurately capture the geometry of the pore space. Standard LBM approaches rely on uniform meshes; adaptive mesh or local grid refinement strategies are still under development and not yet mature for multiphase applications. Increasing spatial resolution leads to very small time steps to ensure numerical convergence and stability according to the CFL condition [51,52].

Due to these requirements, the code was executed on the bwUniCluster 3.0 cluster architecture, consisting of machines equipped with Intel Xeon Platinum 8358 CPUs, which support large-scale simulations. Between 256 and 768 cores were used on average for the simulations presented in this work.

The novelty of this study lies in the development and implementation

of a customized multiphase LBM solver within the open-source framework OpenLB [38,53], specifically designed for pore-scale simulations in pseudo-realistic micromodels. The solver, based on the Allen–Cahn phase-field formulation, has been extended and optimized ad hoc to ensure stability at high density and viscosity ratios and to enhance interface tracking and boundary condition treatment on irregular geometries. These developments address two major limitations commonly encountered in previous studies: the reliance on overly simplified geometrical configurations and the lack of a robust outflow treatment.

The enhanced implementation enables simulations in complex and heterogeneous rock structures, characterized by porosity values ranging from 0.12 to 0.28 and significant variations in channel width. Such geometrical features lead to local flow trapping regions, affecting both the internal pressure distribution and displacement efficiency, thereby allowing for a more realistic characterization of multiphase flow mechanisms. In addition, consistent treatment of the outflow is ensured up to steady-state conditions, enabling stable and accurate handling of changes in the outgoing phase, an aspect that is often oversimplified or neglected in existing literature.

Overall, this study represents a significant step forward in the application of open-source LBM frameworks to realistic pore-scale problems, introducing a custom multiphase Allen–Cahn solver specifically tailored for complex pore geometries and equipped with a robust strategy for outflow and saturation management. Together, these developments bridge the gap between idealized LBM studies and the inherent complexity of natural porous media, providing a reproducible and physically consistent framework for the numerical investigation of underground gas storage processes.

The paper is organized as follows. Section 2.1 presents the designed 2D micromodels, and the workflow adopted to generate them from micro-CT image. In Section 2.2, the multiphase LBM approach is detailed, and some improvements that have been implemented for this work are presented. Boundary conditions are described in Section 2.3. The characterization and discretization of the considered monophase and multiphase scenarios are reported in Section 2.4. Results and discussion are given in Section 3 for monophase (Section 3.1) and multiphase (Section 3.2) simulations, respectively, along with comparisons with CFD simulations. Main conclusions are drawn in Section 4.

2. Materials and methods

2.1. Generation of micromodels for underground porous media investigation

Three micromodels representative of different pore space geometries (in terms of porosity, tortuosity, equivalent pore radius, etc.) were generated for this work.

The first two devices presented here are Rock-on-a Chip, designed from binarized micro-CT images of two real rock samples (Fig. 1): Ketton carbonate [29,31,32] and Sandstone S2 [28,30]. The image resolution for Ketton and S2 was 3 μm/px and 5 μm/px, respectively. The resulting sample size had to be compatible with the microfluidic chips that are commonly used in laboratory tests [8,9,54]. The micromodels' dimensions were 2 *cm* and 1 *cm* (x and y directions), while the available micro-CT samples spanned only a few millimeters. Consequently, several horizontal sections were extracted and assembled. Each section consisted of binarized data (0 = grains, 1 = pores), as shown in Fig. 2 (a-b). To avoid bias, 80–100 horizontal sections (Fig. 2c) were uniformly sampled from 3D micro-CT dataset. For the Ketton case, surfaces were cut because the bottom part of the sample was very poorly connected (Fig. 2a).

The obtained sections were placed side by side, to create a continuous porous path; to avoid the repetition of regular patterns, the sections were randomly shuffled. To ensure 2D connectivity, the sections were linked together as follows (Fig. 3):

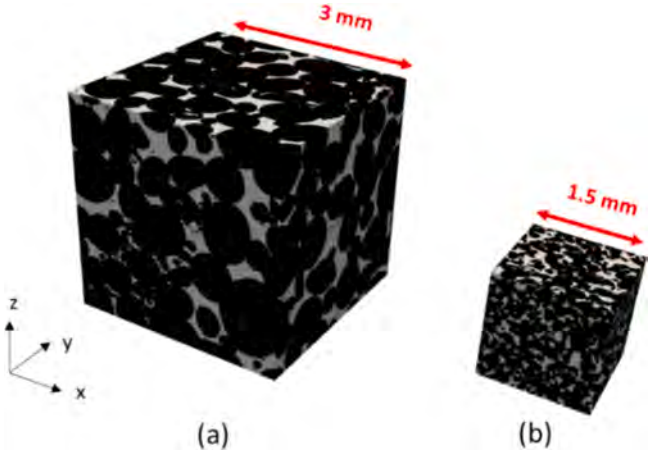

Fig. 1. Binarized micro-CT samples of (a) Ketton carbonate and (b) S2 sandstone (grains in black, pores in white).

1. Insert non-porous spacing of several pixels between adjacent sections (Fig. 3a).
2. Extract and process a subsection across each interface:
   a. Apply dilation with a line kernel along the direction orthogonal to the interface and erosion with a round kernel.
   b. Apply a Gaussian filter to smooth.
   c. Apply a high-pass filter with a threshold of 0.5 to maintain binarization.
3. Improve 2D connectivity:
   a. The skeleton of the porous structure is extracted.
   b. The skeleton is dilated several times to improve connectivity and subsequently thinned out again.
   c. Isolated sections of the skeleton are removed.
   d. The skeleton is dilated to reach the desired minimum channel dimension (Fig. 3b) (45 μm and 15 μm in the Ketton and S2 scenario, respectively).
   e. The skeleton is superimposed on the porous image (Fig. 3c).
4. Remove unconnected pixels.
5. Apply a Gaussian filter to smooth.
6. Apply a high-pass filter with a threshold of 0.5 to binarize the final image (Fig. 3d).
7. Cut the final image to the desired dimension (*2 cm* × *1 cm*).

The resulting geometries used in the simulations are depicted in Fig. 4 for Ketton (a) and S2 (b) scenarios, respectively.

The third device designed and analyzed in this work is a simulated porous rock with a homogeneously distributed pore space generated using a Voronoi tessellation [33]. The Voronoi test case, shown in Fig. 4c, is composed of a regular pattern; however, it presents several criticalities. Because the domain contains narrow channels of approximately 10μm a resolution finer than 4μm is employed in the presented tests. Furthermore, these thin channels yield high capillary pressures (over 8500 Pa, as in [46,55]).

Compared to the other considered devices, the Voronoi geometry is characterized by a relatively low permeability and contains a large number of convex corners, i.e. points where two straight surfaces intersect with a convex angle in the fluid domain. Although the Lattice Boltzmann method is well known for its suitability in handling complex geometries, the accurate treatment of corner points remains non-trivial. These locations introduce ambiguities in the enforcement of fluid–solid boundary conditions, which may affect local momentum exchange, mass conservation, and overall numerical stability [56].

Table 1 summarizes the porosity values of the obtained 2D samples and compares them with the porosity of the corresponding 3D original samples. We remark that the porosity of the 2D micromodels is higher than the 3D samples, especially in the Ketton case, due to the applied 2D

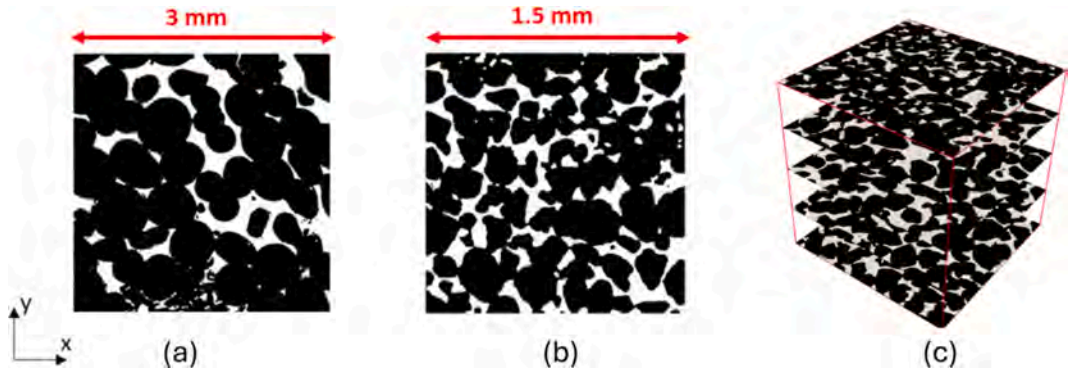

Fig. 2. Example of horizontal sections of (a) Ketton carbonate and (b) S2 sandstone (grains in black, pores in white). Horizontal slices extraction for S2 scenario (c).

connectivity enhancements required for microfluidic device design. Literature permeability values for the considered 3D samples are also reported.

In summary, the three different micromodels analyzed (Fig. 4) exhibit a larger porosity for the Ketton and the S2 test cases, as depicted in Table 1. Differences in tortuosity and pore space geometry affect the flow behavior, and result in different absolute permeability values. These aspects are detailed in Section 3.1, where the permeability values computed through monophase simulation are compared and analyzed.

2.2. Numerical approach using LBM

The numerical approach adopted in this work is the Lattice Boltzmann Method (LBM) [14,56,57], a family of mesoscopic methods that mimic fluid behavior at an intermediate scale between particle-based approaches and macroscopic continuum equations. In LBM, the fluid is represented as a collection of fictitious particles moving on a regular discrete domain, composed of elements called lattices. The flow physics is defined on these lattices [53,58] through a purely local operator that simulates the collision phase of the particles; the choice of an appropriate collision operator depends on the specific flow problem, such as single or multiphase simulations, and plays a crucial role in numerical stability [1,59,60]. After the collision step, the particles propagate during the so-called streaming phase to neighboring lattice cells along a set of predefined velocity directions. This set defines the different numerical schemes used in the literature, denoted by *DdQq*, where $d = \{2, 3\}$ indicates the spatial dimension, and q the number of velocity directions. The scheme applied in this work is *D2Q9,* one of the most widely used [6,56].

Over the years, several multiphase LBM formulations have been proposed, and are still under active development, including the pseudopotential model [42,61–63], colour-gradient model [64–66], free-energy model [41,67], and phase-field model [49,68–71]. Each formulation offers specific advantages and challenges. Phase-field LBM models, based on Allen–Cahn and Cahn–Hilliard equations, have received increasing attention due to their improved numerical stability at high viscosity and density ratios, and their ability to reproduce realistic interface dynamics [26,41,48,49].

The phase-field LBM belongs to the class of diffuse-interface approaches [72], in which the physical properties of the fluid vary smoothly across the interface between phases. The interface has a finite thickness W, and the phases distribution is described by an order parameter ϕ that ranges between 0 and 1, with $\phi = 0$ and $\phi = 1$ corresponding to the two bulk phases. The evolution of ϕ is modeled using either the Cahn-Hilliard or the Allen-Cahn equation [73]. In recent LBM studies, the Allen-Cahn [74–76] formulation has become the preferred alternative, as it provides enhanced numerical stability and robustness, particularly in simulations involving high density ratios. The Allen-Cahn equation [77] can be expressed as:

$$\frac{\partial \phi}{\partial t} + \nabla\cdot(\phi \mathrm{u}) = \nabla\cdot[M(\nabla\phi - \lambda \mathrm{n})], \tag{1}$$

where M is the mobility governing the diffusivity of the phase-function, n is the unit vector normal to the interface, and $\lambda = 4\phi(1-\phi)/W$ rules the contraction in space of the interface.

In addition to the Allen-Cahn equation, the conservation equations of mass and momentum are solved to describe the fluid dynamics. A single set of equations is employed for the mixture, with the different phases distinguished by the order parameter ϕ. The governing equations can be expressed as:

$$\nabla\cdot\mathrm{u} = 0,$$

$$\partial_t(\rho \mathrm{u}) + \nabla\cdot(\rho \mathrm{uu}) = -\nabla p + \nabla\cdot\left[\rho\nu\left(\nabla\mathrm{u} + \nabla\mathrm{u}^T\right)\right] + \mathrm{F}_S + \mathrm{F}_b, \tag{2}$$

where ρ is the fluid density, p the hydrodynamic pressure, μ the dynamic viscosity, F_S the surface tension force, and F_b a possible external body force. The surface tension force is modeled as $\mathrm{F}_S = \mu\nabla\phi$, where μ is the chemical potential $\mu = 4\beta\phi(\phi-1)(\phi-0.5) - \kappa\nabla^2\phi$. Here, β and κ are parameters that depend on the interface thickness W and surface tension σ as: $\beta = 12\sigma/W$ and $\kappa = 1.5\sigma W$.

In the present approach, two coupled LBEs are employed: one to solve the Allen-Cahn equation for the order parameter ϕ, and another to recover the conservation equations of mass and momentum. The LBE corresponding to the Allen-Cahn dynamics can be written as [49]:

$$f_i(\mathrm{x} + \mathrm{c}_i\delta_t, t+\delta_t) - f_i(\mathrm{x}, t) = \frac{1}{\tau_f}\left[f_i(\mathrm{x}, t) - f_i^{eq}(\mathrm{x}, t)\right] + \delta_t F_i(\mathrm{x}, t), \tag{3}$$

where f_i is the distribution function for the momentum equation, f_i^{eq} its equilibrium counterpart, τ_f is the relaxation time and F_i is the forcing scheme responsible for adding the external forces to the method. The variables t and x are the time and space coordinates, respectively. Each index i corresponds to a propagation direction associated with a discrete velocity vector c_i. In this work, these directions are defined according to the D2Q9 lattice [56,57,78]:

$$\mathrm{c}_i = \begin{cases} (0,0), & i = 0, \\ (c,0),\ (0,c),\ (-c,0),\ (0,-c), & i = 1,\ldots,4, \\ (c,c),\ (-c,c),\ (-c,-c),\ (c,-c), & i = 5,\ldots,8, \end{cases}$$

where c is the lattice speed defined as $c = \delta_x/\delta_t$. The parameters δ_x and δ_t are the space and time steps.

The equilibrium distribution function and the forcing term in the Allen-Cahn LBE are defined as follows [49]:

$$f_i^{eq} = w_i\phi\left(1 + \frac{\mathrm{c}_i \bullet \mathrm{u}}{c_s^2}\right),$$

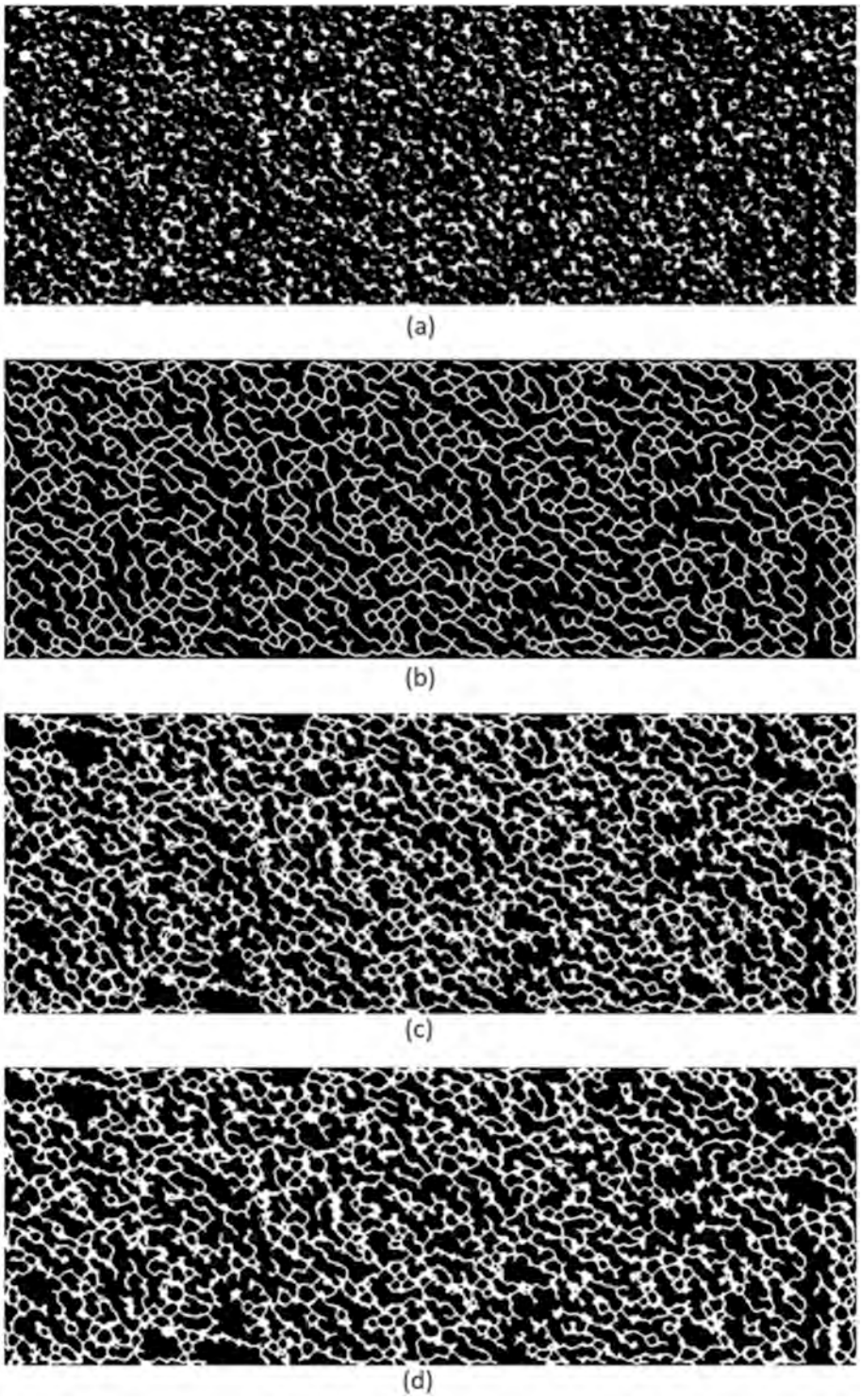

Fig. 3. Workflow from linked sections to final connected image (Ketton scenario; grains in black, pores in white): (a) linked sections (porosity 0.147), (b) connected skeleton, (c) superposition of image and connected skeleton, (d) binarization after Gaussian smoothing (porosity 0.28).

$$F_i = \left(1 - \frac{1}{2\tau_f}\right) \frac{w_i \mathrm{c}_i \bullet \left[\partial_t(\phi \mathrm{u}) + c_s^2 \lambda \mathrm{n}\right]}{c_s^2}, \tag{3.1}$$

where w_i are the weights associated with each velocity c_i. Considering the D2Q9 lattice, these weights are $w_0 = 4/9$, $w_{1,2,3,4} = 1/9$, and $w_{5,6,7,8} = 1/36$. The order parameter is computed from the distribution function:

$$\phi = \sum_i f_i. \tag{4}$$

The mixed fluid density and kinematic viscosity are related to the properties of the two phases and the order parameter:

$$\rho = \phi(\rho_l - \rho_g) + \rho_g,$$

$$\nu = \phi(\nu_l - \nu_g) + \nu_g. \tag{5}$$

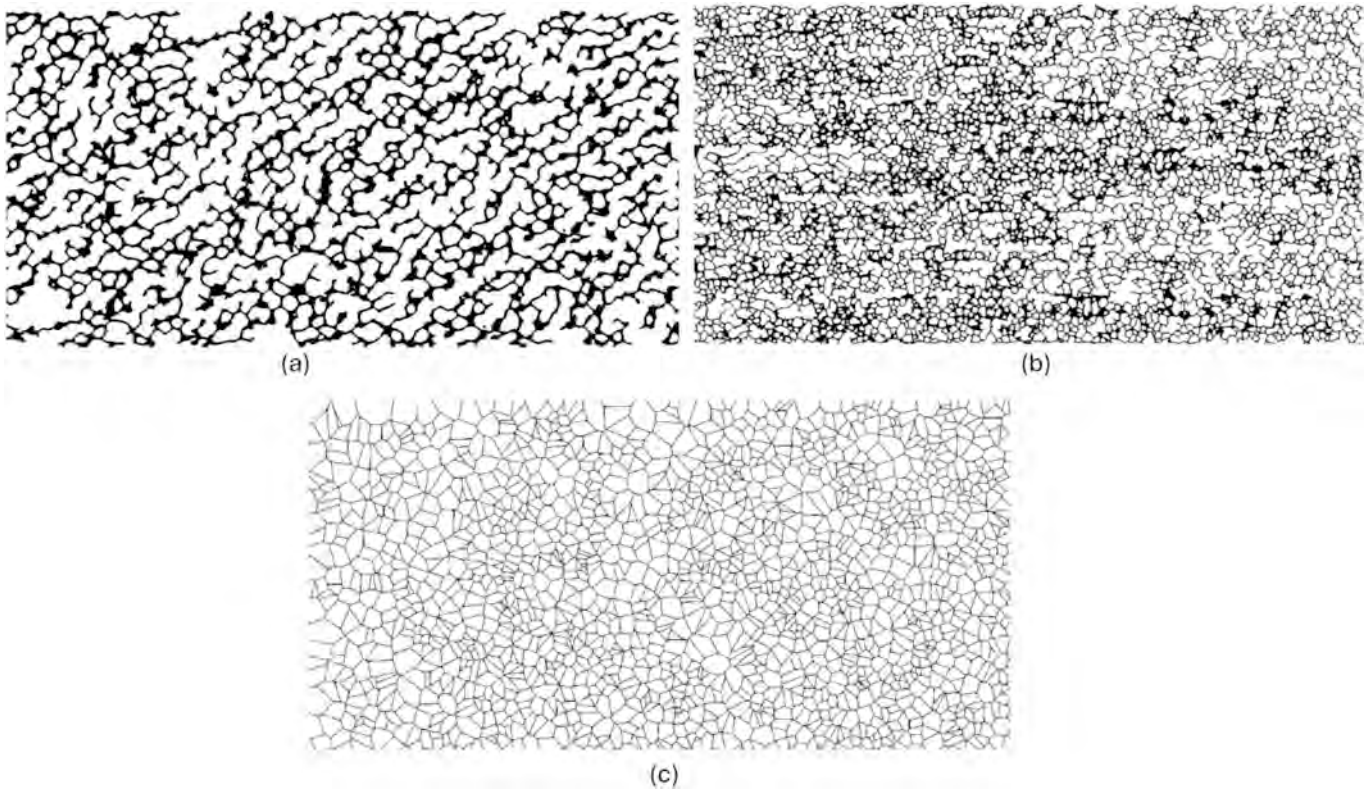

Fig. 4. Ketton (a), S2 (b) and Voronoi (c) 2D micromodels. Black pixels represent the rock pores.

Table 1
Permeability and porosity of the original 3D samples [29,30] compared with the generated 2D geometries.

	Permeability micro-CT 3D (D)	Porosity micro-CT 3D (−)	Porosity 2D geometry (−)
Ketton	5	0.13	0.28
S2	4	0.25	0.27
Voronoi	–	–	0.12

The Navier-Stokes LBE is here based on the formulation proposed by [49]. In the present work, this formulation is adapted to incorporate the regularized collision operator of [79], which is known to provide enhanced numerical stability. It can be written as:

$$g_i(\mathrm{x}+\mathrm{c}_i\delta_t, t+\delta_t) = g_i^{eq}(\mathrm{x},t) + \left(1-\frac{1}{\tau_g}\right)g_i^{(1)} + \delta_t G_i(\mathrm{x},t), \tag{6}$$

with:

$$g_i^{(1)} = w_i\left(-\frac{\delta_t}{2}\mathrm{u}\bullet\nabla\rho - \frac{\delta_t}{2}\frac{\mathrm{c}_i\bullet\mathrm{F}}{c_s^2} + \frac{\mathrm{c}_i\mathrm{c}_i - c_s^2\mathrm{I}}{2c_s^4} : \sum_i\left(\mathrm{c}_i\mathrm{c}_i - c_s^2\mathrm{I}\right)\left(g_i - g_i^{eq}\right)\right), \tag{6.1}$$

where : indicates the double dot product, g_i is the distribution function for the momentum equation, g_i^{eq} its equilibrium counterpart, τ_g is the relaxation time and G_i is a source term. They are defined as (Liang et al. 2018):

$$g_i^{eq} = \begin{cases} \dfrac{p}{c_s^2}(w_i-1) + \rho s_i(\mathrm{u}), & i=0, \\ \dfrac{p}{c_s^2}w_i + \rho s_i(\mathrm{u}), & i\neq 0, \end{cases} \tag{6.2}$$

with

$$s_i(\mathrm{u}) = w_i\left[\frac{\mathrm{c}_i\bullet\mathrm{u}}{c_s^2} + \frac{(\mathrm{c}_i\bullet\mathrm{u})^2}{2c_s^4} - \frac{\mathrm{u}\bullet\mathrm{u}}{2c_s^2}\right], \tag{6.3}$$

and

$$G_i = \left(1-\frac{1}{2\tau_g}\right)w_i\left[\mathrm{u}\bullet\nabla\rho + \frac{\mathrm{c}_i\bullet\mathrm{F}}{c_s^2} + \frac{\mathrm{u}\nabla\rho : \left(\mathrm{c}_i\mathrm{c}_i - c_s^2\mathrm{I}\right)}{c_s^4}\right], \tag{6.4}$$

The macroscopic quantities are computed by (Liang et al. 2018)

$$\rho\mathrm{u} = \sum_i \mathrm{c}_i g_i + 0.5\delta_t\mathrm{F}, p = \frac{c_s^2}{1-\omega_0}\left[\sum_{i\neq 0} g_i + \frac{\delta_t}{2}\mathrm{u}\cdot\nabla\rho + \rho s_0(\mathrm{u})\right]. \tag{7}$$

To further enhance the stability of the method, we adopted the same procedure as in the Smagorinsky LBM [48], where the relaxation time is increased based on the magnitude of the local stress tensor. Smagorinsky method, often used in turbulent flow conditions [48], serve as a general stabilization. It introduces adaptive diffusion in regions characterized by large gradients, thereby increasing dissipation where the flow is under-resolved, thus effectively compensating for insufficient spatial resolution. Standard value for Smagorinsky constant is $C_S = 0.14$ [48]. In this work, a Smagorinsky constant of $C_S = 0.03$ is employed, which was calibrated for the studied geometries and fluids as a tradeoff between stability and introduced diffusion.

All simulations were implemented and executed using the open-source framework OpenLB [38], which was adapted to support the present phase-field formulation.

2.3. Boundary and initial conditions

Due to the significant number of simulations and the heavy computational time, numerical investigations have been carried out adopting 2D geometries, where the third not-described dimension represents the thickness.

No-slip boundary conditions are imposed at the pore walls

(represented in pink in Fig. 5a) and at the external walls (represented in green in Fig. 5a).

Constant pressure boundary conditions are imposed at the inlet (blue left points in Fig. 5) and outlet (yellow right points in Fig. 5a), using the classical Zou-He scheme [80]. Flow direction, highlighted by black arrows in Fig. 5a, is the same for drainage and imbibition simulations. In all cases, the imposed pressure difference has to overcome the expected capillary pressure, which can be calculated for the smaller channel as [55]:

$$p_c = -2\sigma cos\theta\left[\frac{1}{h}+\frac{1}{w}\right] \tag{8}$$

where p_c is the capillary pressure, σ is the surface interfacial tension, the contact angle θ is supposed to be the same for all the walls, h and w are respectively the height and the width of the microchannel. The values presented in Table 5 correspond to the 2D simplified equation:

$$p_c = -2\sigma\frac{cos\theta}{w} \tag{9}$$

Constant inlet pressure boundary conditions could induce a significant discontinuity between the lattice cells at the inlet and the adjacent ones; once converted into lattice units, these terms can introduce numerical errors in the calculation of the gradients and the distribution functions described in Section 2.2. For this reason, the target inlet pressure is imposed gradually within several computing collision/streaming steps corresponding to a physical elapsed time shorter than one millisecond.

For the Navier–Stokes LBM, fixed pressure boundary conditions were imposed at the inlet and outlet using the classical Zou–He scheme [80]. For the Allen–Cahn LBM, a constant value of the order parameter (ϕ) was prescribed at the inlet, also using the Zou–He approach, while a convective boundary condition was applied at the outlet.

When the convective boundary is adopted, it is assumed that the variable of interest (here, ϕ) is advected towards the outflow boundary according to the local fluid velocity. Following [81] formulation, different definitions for the characteristic velocity in the convective term have been investigated. Among these, the use of the mean velocity has been found to yield a good compromise between numerical stability and accuracy. Numerically, the value of ϕ at the outlet boundary node, denoted ϕ_{out}, is computed from the value at the adjacent inner layer ϕ_{in}, according to:

$$\phi_{out}(t+\delta_t) = \phi_{out}(t) + \frac{u_m\delta_t}{\delta_x}(\phi_{out}(t) - \phi_{in}(t)) \tag{10}$$

where u_m represents the mean velocity at the outlet. This formulation effectively allows the order parameter (or any advected scalar) to exit the computational domain smoothly, minimizing reflections and ensuring stable convergence.

An artificial buffer zone is introduced at the inlet, filled with the injected fluid at the beginning of the simulation (blue vertical bandwidth in Fig. 5b, representing water for an imbibition scenario). This assumption mimics laboratory pumps injecting fluid into the micromodel. The resident fluid (hydrogen in Fig. 5b, represented in red) covers the rest of the micromodel.

For numerical stability, a buffer zone is also implemented at the outlet (red vertical bandwidth in Fig. 5b), as the fluid outflowing from the pore structure generates vortices and bubbles that can affect the numerical method if the numerical domain stops immediately after the pore geometry. In this area, the fluid viscosity is gradually increased, and the surface tension force is reduced. This strategy improves the numerical stability when bubbles leave the computational domain, as it prevents spurious disturbances from re-entering and affecting the flow field inside the domain.

2.4. Scenarios

2.4.1. Single-phase

The single-phase simulations presented in this work aim to characterize the absolute permeability through the estimated velocities of the fluid flow. The micromodels were considered fully saturated with water under standard conditions. The fluid was characterized by a density of $\rho = 1000\ kg/m^3$ and a kinematic viscosity v=1e−6 m^2/s. A fixed pressure difference Δp was imposed between inlet and outlet boundaries, corresponding to a pressure gradient of 50 Pa/cm.

The domain discretization represented a compromise between computational cost and the solution accuracy, requiring a sufficient number of fluid cells along the channel section (6 to 10). A comparison with a finer grid resolution was also carried out to verify that the presented results are independent of mesh resolution. Mesh discretization details are summarized in Table 2, while time discretization and computational resources are listed in Table 3. For each geometry, the total number of cells of the computational domain (N_t) is listed together with the number of cells occupied by fluid (N), i.e. the porous domain and the artificial buffer zones introduced next to the inlet and the outlet, the number of fluid cells of the porous domain only (N_p), the number of wall nodes (N_w), i.e. cells at the grain-pore interface or at the pore-external wall interface where bounce-back was applied, and the sum of input and output cells (N_{io}), where pressure boundary conditions were applied. The extent of the inlet and outlet bandwidth can be quantified as $N - N_p$ lattice cells. The refined meshes naturally required a

Table 2
Mesh discretization adopted in the monophase simulations.

Scenario	L_x (cm)	dx (μm)			
		OpenFOAM	OpenLB monophase		OpenLB multiphase
			refined mesh	baseline mesh	
Voronoi	1	1.99	–	1.67	1.67
S2	2	4.79	1.88	3.76	3.76
Ketton	2	4.67	2.08	4.17	4.17

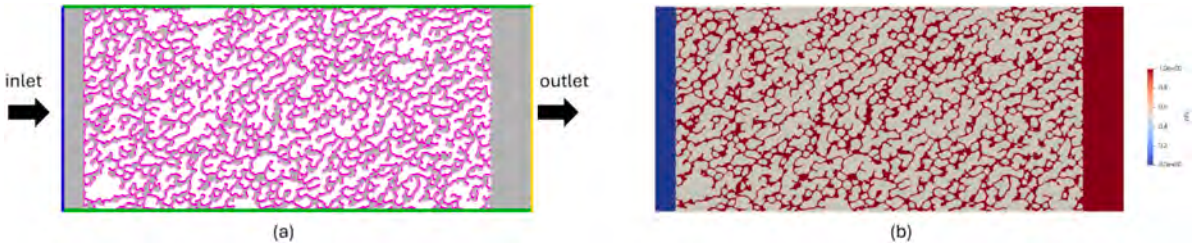

Fig. 5. (a) Boundary condition sketch: external walls (green points) and rock walls (pink points) are considered no-slip; at the inlet (blue points) and the outlet (yellow points), a fixed pressure condition is imposed. Flow direction, which is the same for drainage and imbibition simulations, is highlighted by black arrows. (b) Initial distributions of fluids (ϕ): resident fluid (red, ϕ = 1) and injected fluid (blue, ϕ = 0). (For interpretation of the references to colour in this figure legend, the reader is referred to the web version of this article.)

Table 3
OpenLB discretization computational resources for the monophase simulations.

	Voronoi	S2		Ketton	
		refined mesh	baseline mesh	refined mesh	baseline mesh
N_t	4.36e+06	2.40e+07	6.43e+06	1.67e+07	4.36e+06
N_p	2.27e+06	1.79e+07	4.48e+06	1.29e+07	3.27e+06
N	3.55e+06	2.22e+07	5.57e+06	1.60e+07	4.03e+06
N_w	8.04e+05	1.74e+06	8.54e+05	6.44e+05	3.21e+05
N_{io}	6e+3	1.12e+4	5.6e+3	9.6e+3	4.8e+3
Threads	384–512	768	768	768	384
dt (s)	1.85e-09	2.35e-09	9.42e-09	2.9e-09	1.16e-08

significantly larger number of lattice cells compared to the baseline grids, resulting in increased memory usage, smaller time steps according to Eq. (15) and greater computational effort. Parallel computations were performed using from 384 up to 768 threads for the most demanding cases; details are reported in Table 3.

For the Voronoi scenario, due to the reduced channel size, the resulting cell length was less than 2 μm (see Table 2), which corresponded to over 7 million cells. Considering the high computational cost on one hand and the regularity of the pattern on the other, only a subsection of ¼ of the full domain (1 cm × 0.5 cm) was simulated for this scenario. Furthermore, the refined mesh was not applied to this domain.

For validation purposes, the monophase LBM results were compared to both the OpenFOAM CFD and to the multiphase LBM simulation results, where the injected fluid was set equal to the resident fluid. To ensure fair comparison, very similar discretization between LBM and OpenFOAM were adopted. Unfortunately, we did not have the possibility to run the OpenFOAM simulations on the same cluster used for LBM; therefore, a slightly larger OpenFOAM cell size was adopted to meet memory and computational constraints. Mesh discretization details are compared in Table 2.

The OpenFOAM discretization process of the porous area involved three main steps. First, the block mesh was defined, specifying the investigation area (Table 2) and the hexahedral cell sizes. Then, the castellated mesh was generated using an STL file of the porous structure, which was derived from the binary image of the porous area. No refinement was applied. Finally, a linear extrusion along the z-direction was performed to match the cell height with that of the real microchip. The porous area was connected to two fictitious reservoirs at the inlet and the outlet, each 540 μm in length. At the inlet and outlet boundaries, a fixed pressure value was imposed, and a zero gradient condition was set for the velocity field. No pressure flux and no slip velocity conditions were imposed on the pore walls. The front and back patches on the z axes were set as “empty”, resulting in a 2D simulation in the xy-plane.

Simulations were performed under incompressible conditions using the SIMPLE (Semi-Implicit Method for Pressure Linked Equations) algorithm to solve the Navier-Stokes equations. Pressure and its correction were computed through the GAMG (Geometric-Algebraic Multi-Grid), and Gauss-Seidel was selected as a smoother (sparse linear solver) for both the pressure and velocity fields.

Once the steady state was reached, the permeability was assessed from both LBM and OpenFOAM velocity maps by applying Darcy's law:

$$\kappa = \frac{q}{A}\frac{\mu L}{\Delta p} = u^{*}\frac{\mu L}{\Delta p}. \tag{11}$$

where u^{*} is the Darcy's velocity, μ is the dynamic viscosity, L is the total length of the sample along the x-axis, and Δp is the pressure gap between the inlet and the outlet of the chip.

Darcy velocity was estimated as follows:

1. $N_s = 1000$ equispaced domain slices, orthogonal to the flux direction (along the x-axis), were selected.
2. For the i-th slice S_i identified by $x = x_i$ and area A_i, the local rate was approximated as

$$q_i = \int_{Si} u_x(x_i, y)dA \tag{12}$$

and the Darcy velocity u^{*} was estimated as

$$u^{*} = \frac{1}{N_s}\sum_i \frac{q_i}{A_i}\ . \tag{13}$$

3. Given the uniform discretization, $A_i = N_{pi}\,dA$, thus Eq. (13) corresponds to computing the average of the point-wise velocity values in the pore domain

$$u^{*} = \frac{1}{N_s}\sum_{i=1}^{Ns}\frac{1}{N_{pi}}\sum_y u_x(x_i, y) \tag{14}$$

where N_{pi} is the number of pore cells in the slice S_i.

2.4.2. Two-phase

In the two-phase scenarios, drainage and imbibition tests were simulated for each of the three considered geometries. The wetting fluid was brine, while the non-wetting fluid was gas, either hydrogen, methane, or carbon dioxide. For validation purposes, results of the imbibition scenario in the hydrogen-saturated Ketton scenario were compared with the corresponding multiphase OpenFOAM CFD simulation.

All the scenarios considered were simulated at reservoir conditions, with a pressure of 100 bar and at a temperature of 50 °C. The fluid properties are summarized in Table 4, while the gas interactions with brine are reported in Table 5. Surface tension values were based on experimental results from [82]. The physical range for the contact angles for the studied cases is between 30° and 40° [83]; here, a value of 40° was imposed for all the cases. The expected capillary pressures were analytically calculated from Eq. (9), considering the smallest capillary radius in the domain. p_c values were used to set a feasible pressure difference between inlet and outlet. It is worth noting that the density ratio between hydrogen and brine exceeds two orders of magnitude (Table 4); therefore, this work falls within the category of studies addressing multiphase flow problems involving fluids with large density ratios [45,47,49,84].

Computational time for the multiphase simulations was significantly higher for both CFD and LBM approaches. In addition, the monophase simulations proved that Voronoi permeability is significantly lower than that of the other designs (see Section 3.1). Consequently, only a subsection corresponding to 1/16 of the original Voronoi domain (0.5 cm × 0.25 cm) was simulated; this subsection is depicted in Fig. 6. Therefore, the horizontal lengths of the simulated domains were $L_x = 0.5$ cm for Voronoi and $L_x = 2$ cm for both S2 and Ketton. Nevertheless, due to its regular pattern, we assumed that the saturation results in Section 3.2 were representative of the entire Voronoi domain and that the outflow time could be reasonably scaled by considering the fourfold increase in length. A mesh coarsening was applied for the multiphase simulations for all scenarios (Table 6). The adopted spatial resolutions, ranging from 2.5 μm for Voronoi scenarios to 6.25 μm for Ketton scenarios,

Table 4
Fluid properties in reservoir conditions ($p = 100$ bar, $T = 50$ °C).

	Density (kg/m^3)	Viscosity (Pa s)	Kinematic viscosity (m^2/s)
H_2	*7.1*	*9.50e-06*	*1.34e-06*
CO_2	*384.33*	*2.78e-05*	*7.24e-08*
CH_4	*66.596*	*1.41e-05*	*2.12e-07*
H_2O (brine)	*992.31*	*5.49e-04*	*5.53e-07*

Table 5
Brine-gas fluid interactions under reservoir conditions (p = 100 bar, T = 50 °C).

	Contact angle (°)	Interfacial tension (N/m)	Capillary pressure (Pa)		
			Voronoi (w_{min}~10 μm)	S2 (w_{min}~30 μm)	Ketton (w_{min}~32 μm)
H_2	*40°*	*0.0595*	*9115.93*	*3038.64*	*1519.32*
CO_2	*40°*	*0.0435*	*6664.59*	*2221.53*	*1110.76*
CH_4	*40°*	*0.0568*	*8702.26*	*2900.75*	*1450.38*

corresponded to pore cells in the range N_p = 2.6e+5 – 4.4e+6. The total number of simulated cells (N_t), the number of active fluid cells including the lateral buffers (N), the wall nodes (N_w) and the inlet/outlet boundary nodes (N_{wio}) are detailed in Table 7.

The timestep length was constrained by the CFL condition [51] to ensure convergence and accurate tracking of the advancing interface between the two fluids. In the case of OpenFOAM, an adaptive time step length, ranging from 10e-9 s to 10e-6 s, was used, ensuring a maximum CFL number less than 0.2. LBM simulations employed a fixed time step length, expressed in lattice units as:

$$dt = {c_s}^2(\tau_l - 0.5)\cdot\frac{dx^2}{\nu_l} \quad , {c_s}^2 = 3 \; for \; D2Q9 \tag{15}$$

where dx is the spatial resolution, ν_l is the kinematic viscosity of the liquid, ${c_s}^2$ is the sound speed and τ_l is the relaxation parameter of the collisional operator. Spatial and temporal discretization were tuned to satisfy a maximum CFL number of 0.3 [51], obtaining $\tau_l = 0.502$ for Ketton geometry and $\tau_l = 0.504$ for both the Voronoi and S2 geometries. Space and time discretization details are summarized in Table 6.

For the two-phase OpenFOAM simulation, the incompressible Volume of fluid (VoF) method was applied, solving the phase fraction equation in each computational cell to determine the local relative volume fraction of the two phases. The PIMPLE algorithm was applied to solve the Navier-Stokes equations. Pressure and its correction were again computed through the GAMG solver associated with a Gauss-Seidel smoother. Velocity and phase fraction were calculated through a symmetric Gauss-Seidel smoother.

Due to the complexity of the domain, the multiphase computational effort required on each lattice cell, and the high contrast between fluid properties, the computational cost was significant, and an efficient parallel distribution was essential. For the LBM simulations, we used the bwUniCluster 3.0 architecture, consisting of machines equipped with Intel Xeon Platinum 8358 CPUs capable of supporting large-scale simulations. On average, between 384 and 512 physical cores were employed, with each core corresponding to a separate computational process (Table 7). As an example, a distribution among 512 processes for the Ketton domain is shown in Fig. 7.

The computation was stopped when the distribution of the two fluids no longer changed significantly over successive timesteps.

The number of cells occupied by the injected fluid N_f was computed to evaluate the saturation of the injected fluid as:

$$S_f = N_f / N_p \tag{16}$$

where N_p is the number of porous cells.

3. Results and discussion

In this section, the results of the simulations performed on the micromodels are presented and discussed. Section 3.1 details the results of the single-phase simulations, which were analyzed to assess the absolute permeability of each scenario, and compared with the values estimated from OpenFOAM velocity fields. Section 3.2 presents the two-phase OpenLB simulations of drainage and imbibition tests, considering brine and three different gases: hydrogen, methane, and carbon dioxide. A comparison with OpenFOAM results for the imbibition scenario of the hydrogen-saturated Ketton domain is also provided.

Table 6
Discretization parameters and imposed pressure drop (inlet–outlet) for the two-phase scenarios.

	Voronoi	S2	Ketton	
			OpenLB	OpenFOAM
L_x (cm)	0.5	2	2	2
dx (μm)	2.5	3.76	6.25	9.33
N_p	2.6e+5	4.4e+6	1.4e+6	7.5e+5
dt (s)	1.51e-8	3.41e-8	4.71e-8	10e-9 to 10e-6
Δp (Pa)	4e+4	5e+4	8.5e+3	8.5e+3

Table 7
Computational details for the two-phase OpenLB simulations.

	Voronoi	S2	Ketton
N_t	6.78e+05	7.57e+06	3.66e+06
N	5.43e+05	6.71e+06	3.44e+06
N_w	1.33e+05	8.55e+05	2.16e+05
N_{io}	2e+3	5.6e+3	3.2e+3
Threads	384	512	512

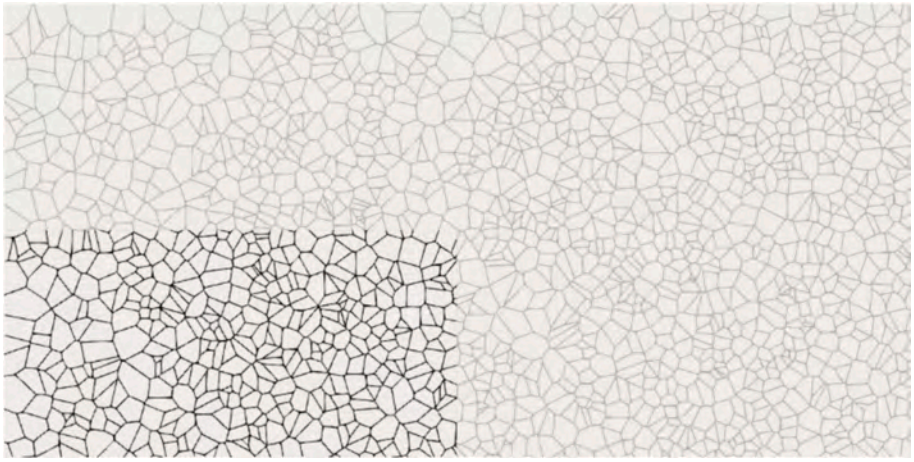

Fig. 6. Voronoi subset (black) used as porous domain in two-phase flow simulation. The porous area simulated in the monophase scenario shown in light grey.

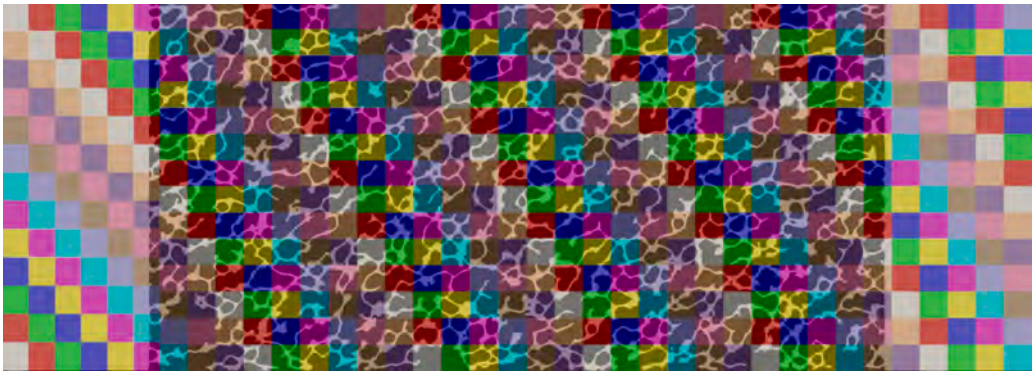

Fig. 7. Ketton domain distribution among 512 cores, adopted for multiphase simulation. The domain subset assigned to each core is represented by a colored rectangle.

3.1. Single-phase simulations

Comparison of permeability estimates among OpenFOAM and OpenLB simulations, considering single-phase vs. multiphase approaches and different meshes (Section 2.4.1), is summarized in Table 8. A good level of consistency is observed between the single-phase LMB solver and the multiphase LBM solver for all considered scenarios. Furthermore, the results obtained using the baseline and refined meshes were in agreement, confirming that the presented LBM results were not biased by the discretization length.

The permeability values obtained from the OpenFOAM solver were systematically higher, but in the same order of magnitude, than those obtained using the single-phase LBM approach, with discrepancies increasing for narrower-channel geometries such as the Voronoi scenario. These differences may primarily arise from the different approximations of the original domain image adopted by the two approaches, as their meshing routines differ, and the imposed cell size in the OpenFOAM simulations was slightly larger (Table 2). As a consequence, the OpenFOAM meshes were characterized by slightly wider channels, corresponding to a small increase in porosity, an effect that becomes non-negligible in low porosity scenarios. The relative discrepancy ranged from 0.05% for the Ketton scenario, to 8.6% for the S2 scenario and 16% for the Voronoi domain. Differences arising from adaptive vs. fixed time discretization may also have an impact. Nevertheless, both methods yielded permeability estimates of the same order of magnitude.

It is worth noting that, compared with the original 3D micro-CT samples (Table 1), the 2D geometry generated from Ketton was characterized by higher permeability values, while the 2D geometry based on Sandstone S2 did not show significant changes. The Voronoi geometry, instead, exhibited a relatively low permeability (Table 8).

3.2. Two-phase simulations

Preliminary, a validation through the comparison between the OpenFOAM CFD simulation and the multiphase OpenLB LBM model is provided for the imbibition scenario of the Ketton geometry filled with hydrogen. The focus is placed on the fluid distribution obtained at three different time frames: the stationary time, (i.e. the time after which the fluid distribution does not change anymore), the outflow time, (i.e. the time the injected fluid reaches the right end of the porous domain and enter the right artificial buffer zone, represented by a vertical band with $\phi = 1$), and an intermediate time during the simulation (approximately 0.04 s). The effect of flow velocity was not investigated and will be addressed in future work. Fig. 8 compares the evolution of the fluid distribution at intermediate, outflow, and stationary times. The water distributions are comparable, and the same preferential paths are observed. The corresponding physical times and water saturation values are compared in Table 9. The OpenFOAM simulation shows a slightly faster flow, reaching the outflow approximately 0.04 s earlier, and exhibiting a more significant fingering. Minor local discrepancies are observed in the final saturation, see Fig. 9, with some pore regions intruded only in OpenFOAM and others only in OpenLB. These discrepancies can be attributed to differences in time discretization (Table 6), as well as to minor differences in domain meshing (Table 6), which results in a relative porosity discrepancy of 0.25%, in addition to the distinct numerical approaches applied. Nevertheless, the saturation evolution remains consistent between the two simulations.

Results of all the considered multiphase scenarios for the different geometries and brine-gas systems are summarized in Table 11 in terms of outflow time and stationary time, while the final saturations are reported in Table 10. For each scenario, a set of images illustrating the temporal evolution of the saturation maps is reported in the Supplementary Materials. Phase distributions for all drainage scenarios are compared at intermediate time in Fig. 10, at the outflow time in Fig. 11, while all the imbibition scenarios are compared at intermediate time in Fig. 12. In addition, Table 12 reports the corresponding number of LBM iterations associated with both the outflow and stationary times for each geometry and displacement process (drainage and imbibition). This information provides a quantitative indication of the computational effort required to reach these relevant physical observation times.

The results highlight clear differences in displacement behavior, depending on the geometry and the injected/resident fluid combination (Table 10 and Table 11). It is pointed out that, since the length of the Voronoi domain is ¼ of the length of the other geometries, a scaling factor of four must be applied when comparing outflow times with larger domains. Conversely, the saturation values can be compared directly across all geometries because the Voronoi section is considered representative of the whole domain due to its regularity.

Significant viscous fingering, observed during the drainage process (Fig. 10 and Fig. 11), is more pronounced for hydrogen in all the geometries, and becomes more evident in the case characterized by smaller capillary values (i.e., Voronoi and S2 scenarios). In these cases, the gas moves to the outlet more rapidly by following a preferential path, resulting in a markedly reduced fraction of displaced water. However, the regularity of the geometry influences the final saturation more than the gas viscosity. Despite the pronounced fingering, drainage with H_2 in the Voronoi geometry allows a considerable water displacement (final

Table 8
Comparison of estimated permeabilities (D).

Scenario	OpenFOAM single-phase	OpenLB single-phase		OpenLB two-phase
		refined mesh	baseline mesh	
Voronoi	0.83	–	0.28	0.26
S2	16.9	7.6	7.2	5.1
Ketton	33	24	24	20

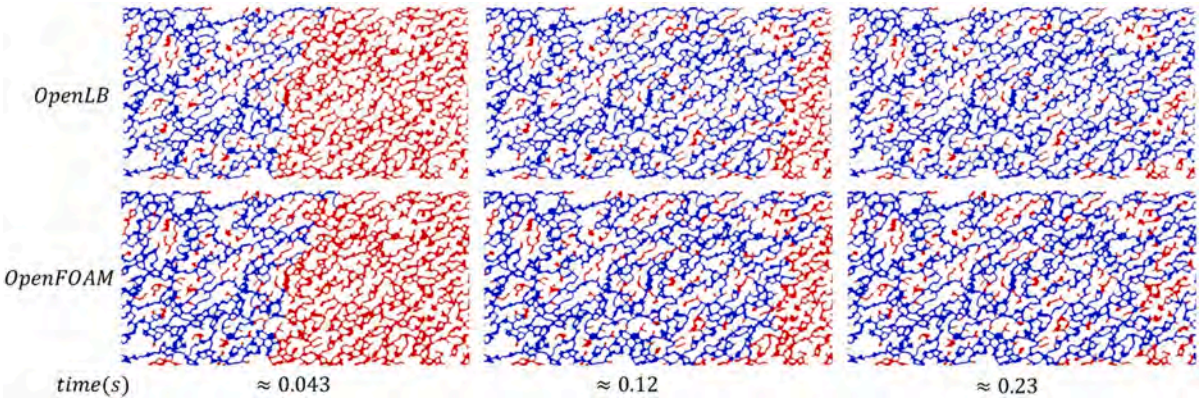

Fig. 8. OpenLB and OpenFOAM hydrogen imbibition fluids distribution at comparable time steps. Water (blue) and gas (red). (For interpretation of the references to colour in this figure legend, the reader is referred to the web version of this article.)

Table 9
Comparison of saturation values between OpenLB and OpenFOAM at comparable time steps.

	OpenLB		OpenFOAM	
	t [s]	S_w	t [s]	S_w
Intermediate time	0.047	0.39	0.04	0.39
Outflow time	0.148	0.76	0.11	0.7
Stationary time	0.184	0.85	0.2	0.77

gas saturation of 0.799), whereas in the Ketton geometry, characterized by highly variable channel diameters and a significant portion of interrupted porous paths, the final gas saturation reaches only 0.492.

In the context of gas storage in aquifer, the viscous fingering observed during drainage, especially for hydrogen, leads to limited sweep efficiency and potentially significant hysteresis effects during cyclic operation. Therefore, in conventional UGS, and in particular in UHS and CO2 storage, analysis of micro-scale phenomena has to be considered for the definition of the reservoir management strategy, dynamic modelling, calculation of storage capacity, design of injection/production schedule and, probably, even in storage site selection.

In contrast, the imbibition process exhibits a more piston-like displacement across the samples in all cases (Fig. 12). The higher the viscosity of the resident gas (e.g., CO_2), the slower the imbibition of the sample. Furthermore, for geometries characterized by small pores (i.e., the Voronoi and S2 scenarios) initially saturated with H_2, the advancing water front is substantially less uniform, and the fraction of non-displaced gas is non-negligible, resulting in reduced final water saturation values (Table 10). This behavior is associated with capillary fingering: the invading fluid does not progress continuously, but instead 'jumps' between larger pores, following pathways with lower capillary entry pressure. This can lead to significant gas capillary trapping.

In the context of underground gas storage, significant capillary fingering may reduce the volume of effectively recoverable working gas.

The described phenomena are in good agreement with the Lenormand diagram, reported in Fig. 13, which shows that viscous fingering should occur in drainage scenarios, more severely for hydrogen, that exhibit the lowest viscosity ratio ($M = \mu_{inj}/\mu_r$). Conversely, capillary fingering is expected to dominate the imbibition process, especially for hydrogen and for the Voronoi scenarios.

4. Conclusions

This work focuses on the application of an Allen-Cahn LBM formulation with dedicated boundary conditions, implemented in the OpenLB library, to simulate multiphase flow at the pore scale. To ensure numerical convergence, the Smagorinsky model is adopted, with the relaxation time adjusted accordingly. A series of imbibition and drainage simulations for water/gas systems (H_2, CH_4, and CO_2) on tailored 2D micromodel (Rock-on-a-Chip) designs, with different porosity and tortuosity values, are presented and discussed.

A preliminary single-phase validation of LBM against CFD solver provided a characterization of absolute permeability values for the analyzed domains. Subsequently, two-phase flow simulations demonstrated that the proposed LBM implementation effectively captures pore-

Table 10
Injected fluid saturation at the stationary time.

	Drainage Saturation of gas			Imbibition Saturation of water		
	H_2	CH_4	CO_2	H_2	CH_4	CO_2
Voronoi	0.799	0.726	0.712	0.553	0.905	0.972
S2	0.448	0.611	0.613	0.645	0.880	0.982
Ketton	0.492	0.523	0.530	0.846	0.825	0.784

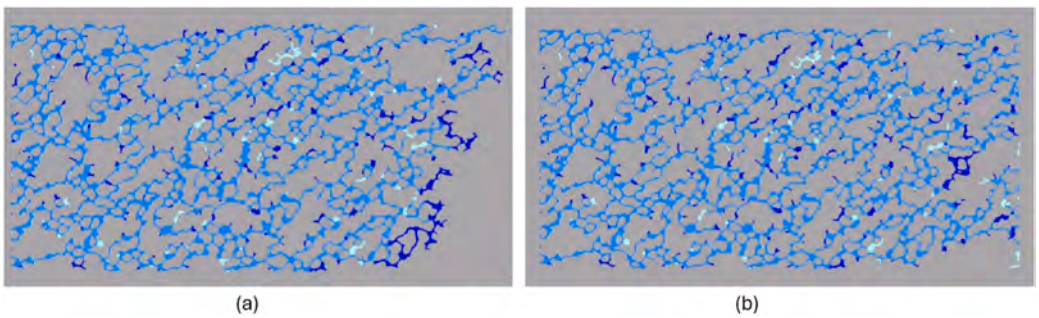

Fig. 9. Water map overlays: LBM (dark blue) vs. OpenFOAM (light blue) at (a) outflow time and (b) stationary time. The intermediate tone corresponds to overlapping. (For interpretation of the references to colour in this figure legend, the reader is referred to the web version of this article.)

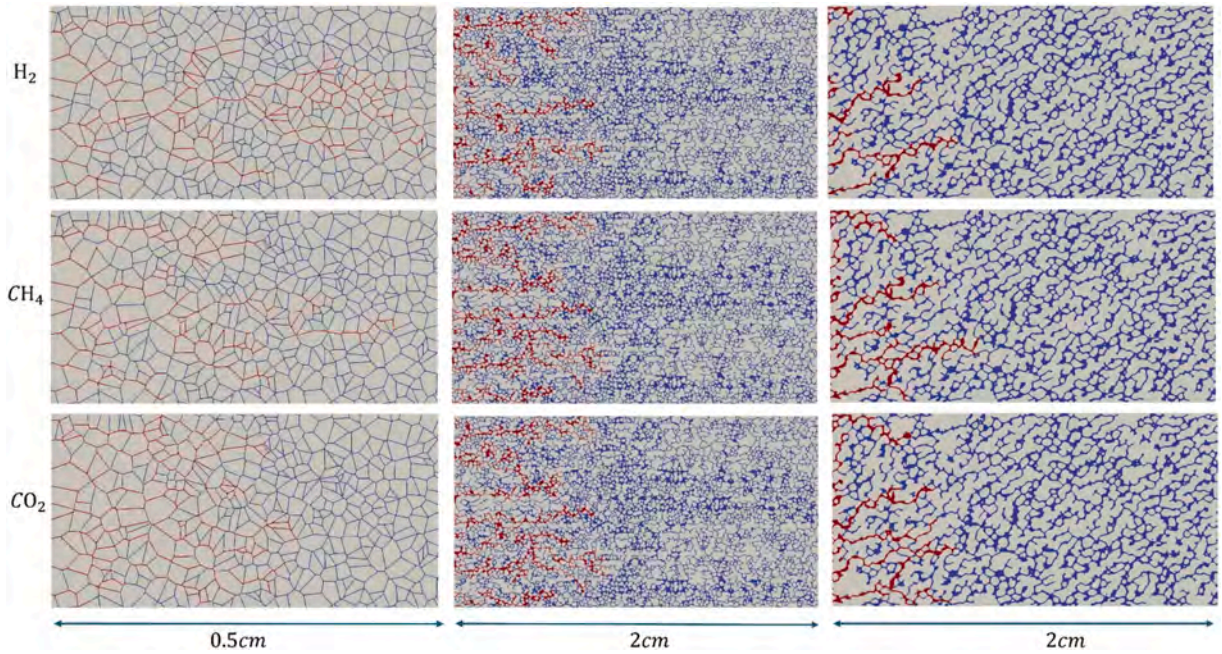

Fig. 10. Comparison of drainage scenarios at an intermediate time (approximately t = 0.04 s). Gas (red) and water (blue). (For interpretation of the references to colour in this figure legend, the reader is referred to the web version of this article.)

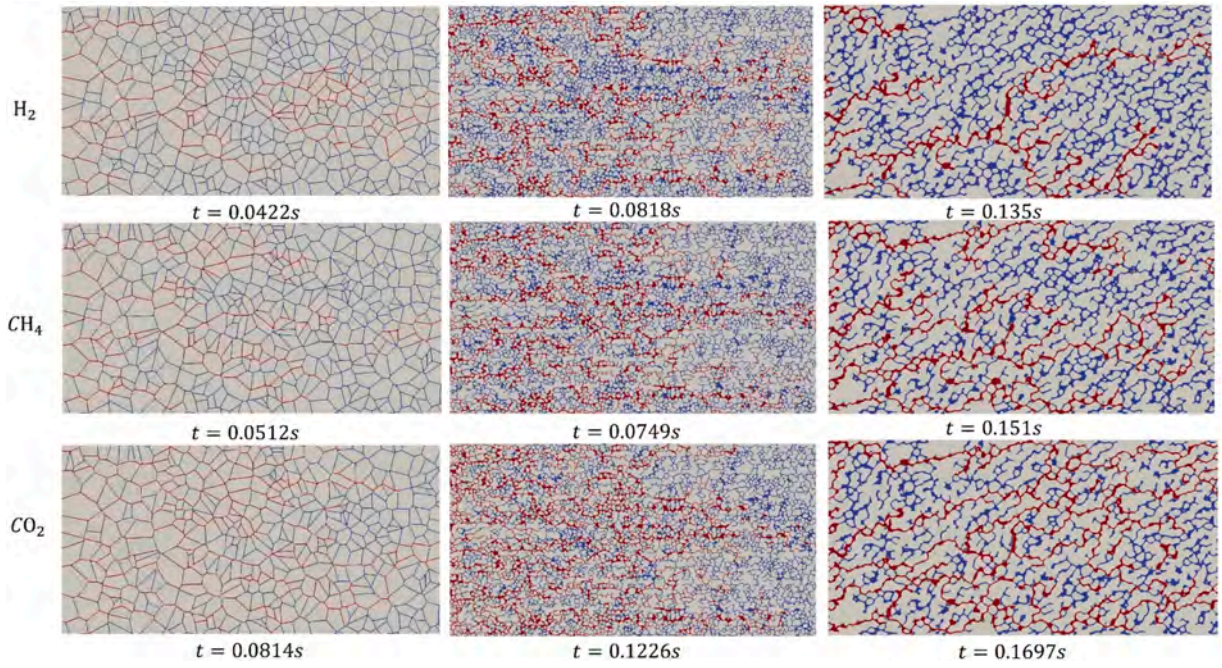

Fig. 11. Comparison of drainage scenarios at outflow times. Gas (red) and water (blue). (For interpretation of the references to colour in this figure legend, the reader is referred to the web version of this article.)

scale displacement dynamics. Geometry effects were clearly observed, confirming the strong influence of pore structure on flow behavior, trapping mechanisms, and residual saturation. The morphology of the simulated fluid-fluid displacement patterns is consistent with the Lenormand diagram, with pronounced viscous fingering during drainage, especially for hydrogen scenarios, and more stable displacement during imbibition, except for the Voronoi geometry in the hydrogen case, which is more affected by capillary fingering.

A representative imbibition test was validated against OpenFOAM CFD solver, showing overall agreement in results with only minor local discrepancies. Furthermore, the tests confirmed the robustness of the adopted computational strategy, i.e. the adaptive relaxation time and the tailored boundary conditions, which ensured stable simulations even under reservoir conditions and high density ratios.

Overall, this study demonstrates that the proposed implementation can provide valuable insights into pore-scale simulation of underground storage of hydrogen, methane, and carbon dioxide. These results have direct implications for reservoir-scale dynamics, as pore-scale displacement mechanisms control macroscopic parameters such as residual and critical saturations, capillary forces, and relative

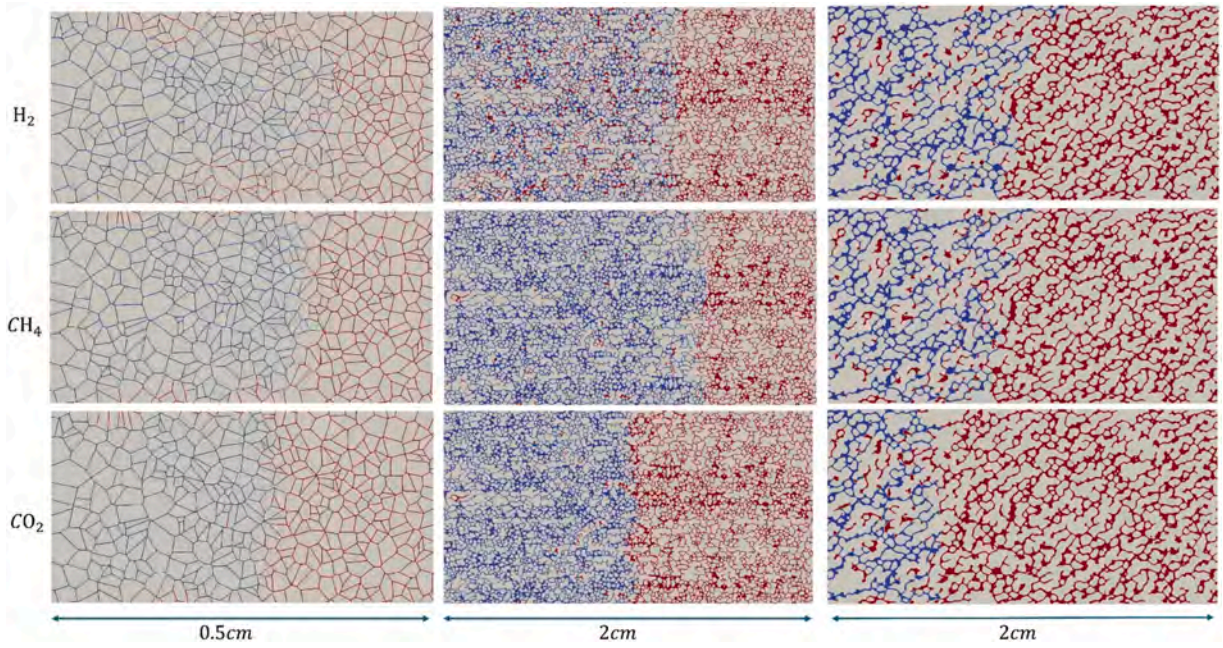

Fig. 12. Comparison of imbibition scenarios at an intermediate time (approximately $t = 0.04$ s). Gas (red) and water (blue). (For interpretation of the references to colour in this figure legend, the reader is referred to the web version of this article.)

Table 11
Comparison of simulations relevant times.

	Geometry	Drainage			Imbibition		
Gas		H_2	CH_4	CO_2	H_2	CH_4	CO_2
Outflow time (s)	Voronoi	0.042	0.051	0.081	0.065	0.087	0.106
	S2	0.082	0.075	0.123	0.068	0.089	0.109
	Ketton	0.135	0.151	0.169	0.148	0.160	0.227
Stationary time (s)	Voronoi	0.362	0.151	0.151	0.128	0.452	0.151
	S2	0.170	0.245	0.23	0.068	0.102	0.170
	Ketton	0.472	0.490	0.919	0.471	0.236	0.566

Table 12
LBM iterations associated with relevant times.

	Geometry	Drainage			Imbibition		
Gas		H_2	CH_4	CO_2	H_2	CH_4	CO_2
Outflow LBM iterations	Voronoi	2.79e+06	3.40e+06	5.40e+06	4.30e+06	5.80e+06	7.00e+06
	S2	2.00e+05	2.20e+06	7.20e+06	2.00e+06	2.60e+06	3.20e+06
	Ketton	2.90e+06	3.20e+06	3.60e+06	3.00e+06	3.40e+06	4.80e+06
Stationary LBM iterations	Voronoi	2.40e+07	1.00e+07	1.00e+07	8.50e+06	3.00e+07	1.00e+07
	S2	5.00e+06	7.20e+06	13.5e+06	2.00e+06	3.00e+06	5.00e+06
	Ketton	1.00e+07	1.04e+07	1.95e+07	1.e+07	5.00e+06	1.20e+07

permeabilities, which are crucial for designing effective underground storage management strategies.

CRediT authorship contribution statement

Alice Raeli: Writing – review & editing, Writing – original draft, Visualization, Validation, Software, Resources, Methodology, Data curation, Conceptualization. **Eloisa Salina Borello:** Writing – review & editing, Writing – original draft, Visualization, Software, Resources, Data curation, Conceptualization. **Cristina Serazio:** Writing – review & editing, Validation, Software, Resources, Data curation. **Luiz Eduardo Czelusniak:** Writing – review & editing, Validation, Software, Resources, Methodology. **Tim Niklas Bingert:** Software. **Mathias J. Krause:** Writing – review & editing, Software, Resources, Project administration, Methodology. **Dario Viberti:** Writing – review & editing, Validation, Supervision, Project administration, Methodology, Conceptualization.

Code availability

The simulations in this study were carried out using the OpenLB library, an open-source framework for lattice Boltzmann simulations. The source code and documentation are freely available at https://www.openlb.net/, and the latest release can be accessed at https://gitlab.com/openlb/release.

An example code enabling full reproducibility of the tests and results reported in this work is provided within the OpenLB distribution under the folder: examples/porousMedia/gasStorage2d.

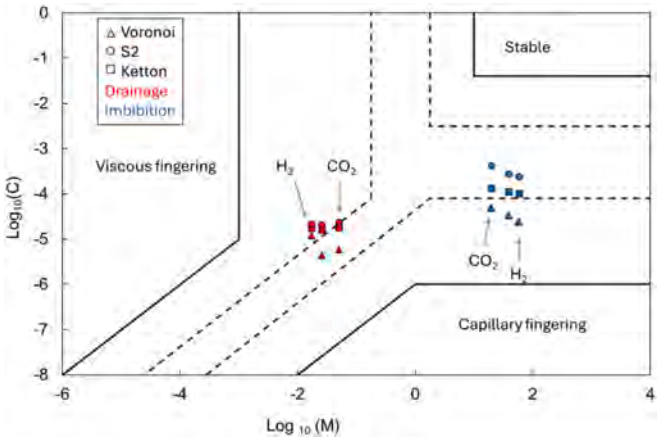

Fig. 13. Lenormand diagram, where the solid lines represent the originally proposed boundaries [85] and dashed lines are boundaries proposed by [86].

Declaration of competing interest

The authors declare that they have no known competing financial interests or personal relationships that could have appeared to influence the work reported in this paper.

Data availability

The software used for this work is open source with home-made optimizations. The models are home-made from data available online and available on request

Acknowledgements

Project funded by the European Union – NextGenerationEU under the National Recovery and Resilience Plan (NRRP), Mission 04 Component 2 Investment 3.1 | Project Code: IR0000027 - CUP: B33C22000710006 - iENTRANCE@ENL: Infrastructure for Energy TRAnsition aNd Circular Economy @ EuroNanoLab. Views and opinions expressed within the document are, however, those of the author(s) only and do not necessarily reflect those of the European Union or the European Commission. Neither the European Union nor the Commission can be held responsible for them.

The authors acknowledge support by the state of Baden-Württemberg through bwHPC.

Appendix A. Supplementary data

Supplementary data to this article can be found online at https://doi.org/10.1016/j.est.2026.121868.

References

[1] M.J. Blunt, Multiphase Flow in Permeable Media: A Pore-scale Perspective, 2017.
[2] B. Ghanbarian, A.G. Hunt, R.P. Ewing, M. Sahimi, Tortuosity in porous media: a critical review, Soil Sci. Soc. Am. J. 77 (2013) 1461–1477, https://doi.org/10.2136/sssaj2012.0435.
[3] C. Benetatos, S. Bocchini, A. Carpignano, A. Chiodoni, M. Cocuzza, C. Deangeli, et al., How underground systems can contribute to meet the challenges of energy transition, GEAM Geoing. Ambient. E Mineraria 58 (2021) 65–80, https://doi.org/10.19199/2021.163-164.1121-9041.065.
[4] F. Panini, B. Ghanbarian, E. Salina Borello, D. Viberti, Estimating geometric tortuosity of saturated rocks from micro-CT images using percolation theory, Transp. Porous. Media (2024), https://doi.org/10.1007/s11242-024-02085-w.
[5] E. Salina Borello, C. Peter, F. Panini, D. Viberti, Application of A* algorithm for microstructure and transport properties characterization from 3D rock images, Energy 239 (2022) 122151, https://doi.org/10.1016/j.energy.2021.122151.
[6] A. Raeli, E. Salina Borello, D. Viberti, Lattice Boltzmann method for pore-scale multi-phase flow simulation in underground porous media: a review, Geoing E Attiv Estrattiva GEAM (2024) 21–36, doi:In%2520press.
[7] A. Raeli, E. Salina Borello, F. Panini, C. Serazio, D. Viberti, A parallel programming application of the A* algorithm in digital rock physics, Comput. Geosci. (2024) 105578, https://doi.org/10.1016/j.cageo.2024.105578.
[8] A. Massimiani, F. Panini, S.L. Marasso, N. Vasile, M. Quaglio, C. Coti, et al., Design, fabrication, and experimental validation of microfluidic devices for the investigation of pore-scale phenomena in underground gas storage systems, Micromachines 14 (2023) 308, https://doi.org/10.3390/mi14020308.
[9] A. Massimiani, F. Panini, S.L. Marasso, M. Cocuzza, M. Quaglio, C.F. Pirri, et al., 2D microfluidic devices for pore-scale phenomena investigation: a review, Water 15 (2023) 1222, https://doi.org/10.3390/w15061222.
[10] A. Kummerländer, M. Dorn, M. Frank, M.J. Krause, Implicit propagation of directly addressed grids in lattice Boltzmann methods, Concurr. Comput. Pract. Exp. 35 (2023) e7509, https://doi.org/10.1002/cpe.7509.
[11] A. Kummerländer, F. Bukreev, D. Teutscher, M. Dorn, M.J. Krause, Optimization of Single Node Load Balancing for Lattice Boltzmann Methods on Heterogeneous High Performance Computers, 2024, https://doi.org/10.2139/ssrn.4713497.
[12] J. Latt, C. Coreixas, J. Beny, Cross-platform programming model for many-core lattice Boltzmann simulations, PloS One 16 (2021) e0250306, https://doi.org/10.1371/journal.pone.0250306.
[13] H. Liu, Q. Kang, C.R. Leonardi, S. Schmieschek, A. Narváez, B.D. Jones, et al., Multiphase lattice Boltzmann simulations for porous media applications: a review, Comput. Geosci. 20 (2016) 777–805, https://doi.org/10.1007/s10596-015-9542-3.
[14] A.J. Wagner, A Practical Introduction to the Lattice Boltzmann Method, 2008.
[15] X. Zhu, S. Wang, Q. Feng, L. Zhang, L. Chen, W. Tao, Pore-scale numerical prediction of three-phase relative permeability in porous media using the lattice Boltzmann method, Int. Commun. Heat Mass Transf. 126 (2021) 105403, https://doi.org/10.1016/j.icheatmasstransfer.2021.105403.
[16] C. Zhao, S.S. Patel, H.L. Lin, M. Min, T. Lee, A flux bounce-back scheme for the filtered spectral element lattice Boltzmann method, Comput. Fluids 308 (2026) 106987, https://doi.org/10.1016/j.compfluid.2026.106987.
[17] D. Wang, F. Liu, J. Sun, Y. Li, Q. Wang, Y. Jiao, et al., Lattice-Boltzmann simulation of two-phase flow in carbonate porous media retrieved from computed microtomography, Chem. Eng. Sci. 270 (2023) 118514, https://doi.org/10.1016/j.ces.2023.118514.
[18] M.C. Sukop, H. Huang, C.L. Lin, M.D. Deo, K. Oh, J.D. Miller, Distribution of multiphase fluids in porous media: comparison between lattice Boltzmann modeling and micro-x-ray tomography, Phys. Rev. E 77 (2008) 026710, https://doi.org/10.1103/PhysRevE.77.026710.
[19] Y. Liu, J. Feng, J. Min, X. Zhang, Homogenized color-gradient lattice Boltzmann model for immiscible two-phase flow in multiscale porous media, J. Appl. Phys. 135 (2024) 184701, https://doi.org/10.1063/5.0202947.
[20] H. Erfani, R. Haghani, J. McClure, E. Boek, C.F. Berg, Spatial characterization of wetting in porous media using local lattice-Boltzmann simulations, Transp. Porous Media 151 (2024) 429–448, https://doi.org/10.1007/s11242-023-02044-x.
[21] Y. Sun, H. Yu, Z. Ren, B. Yang, Z. Li, C. Xu, Pore-scale simulation of three-phase displacement in 3D porous media using advanced LBM: insights into CO2 enhanced oil recovery and storage, Comput. Geotech. 185 (2025) 107346, https://doi.org/10.1016/j.compgeo.2025.107346.
[22] G. Yang, H. Chen, M. Wang, Lattice Boltzmann model for immiscible three-phase flows with phase change, Phys. Rev. E. 111 (2025) 065310, https://doi.org/10.1103/prh3-xhcb.
[23] A. Fakhari, Y. Li, D. Bolster, K.T. Christensen, A phase-field lattice Boltzmann model for simulating multiphase flows in porous media: application and comparison to experiments of CO2 sequestration at pore scale, Adv. Water Resour. 114 (2018) 119–134, https://doi.org/10.1016/j.advwatres.2018.02.005.
[24] D.H. Kang, T.S. Yun, Local hybrid Allen-Cahn model in phase-field lattice Boltzmann method for incompressible two-phase flow, Phys. Rev. E. 105 (2022) 045307, https://doi.org/10.1103/PhysRevE.105.045307.
[25] D.H. Kang, T.S. Yun, Minimized capillary end effect during CO_2 displacement in 2-D micromodel by manipulating capillary pressure at the outlet boundary in lattice Boltzmann method, Water Resour. Res. 54 (2018) 895–915, https://doi.org/10.1002/2017WR021409.
[26] L. Ju, C. Zhang, B. Yan, S. Sun, Phase-field based lattice Boltzmann modeling of contact angles in binary flow with large density ratios, Int. J. Multiph. Flow 195 (2026) 105504, https://doi.org/10.1016/j.ijmultiphaseflow.2025.105504.
[27] D. Sashko, T.R. Mitchell, Ł. Łaniewski-Wołłk, C.R. Leonardi, Phase field lattice Boltzmann method for liquid-gas flows in complex geometries with efficient and consistent wetting boundary treatment, Comput. Math. Appl. 186 (2025) 101–129, https://doi.org/10.1016/j.camwa.2025.03.014.
[28] H. Dong, M.J. Blunt, Pore-network extraction from micro-computerized-tomography images, Phys. Rev. E. 80 (2009) 036307, https://doi.org/10.1103/PhysRevE.80.036307.
[29] M. ANDREW, Reservoir-Condition Pore-Scale Imaging of Multiphase Flow, PhD Thesis, Imperial, London, 2014, p. 666.
[30] Imperial college consortium on pore-scale imaging and modelling, in: Berea Sandstone, 2014, https://doi.org/10.6084/M9.FIGSHARE.1153794.V2, 0 Bytes.
[31] M. Andrew, B. Bijeljic, M.J. Blunt, Pore-scale contact angle measurements at reservoir conditions using X-ray microtomography, Adv. Water Resour. 68 (2014) 24–31, https://doi.org/10.1016/j.advwatres.2014.02.014.
[32] A.Q. Raeini, B. Bijeljic, M.J. Blunt, Generalized network modeling: network extraction as a coarse-scale discretization of the void space of porous media, Phys. Rev. E. 96 (2017) 013312, https://doi.org/10.1103/PhysRevE.96.013312.
[33] G. Voronoi, Nouvelles applications des paramètres continus à la théorie des formes quadratiques. Deuxième mémoire. Recherches sur les parallélloèdres primitifs,

J. Für. Reine Angew. Math. Crelles. J. 1908 (1908) 198–287, https://doi.org/10.1515/crll.1908.134.198.
[34] M. Katzmayr, L. Ganzer, An iterative algorithm for generating constrained voronoi grids 1 (2009) 381–391, https://doi.org/10.2118/118942-ms.
[35] M. Karavelas, 2D Voronoi Diagram Adaptor. CGAL User Ref. Man. 5.2.2, CGAL Editorial Board, 2021.
[36] L. Wang, Z. Peng, Pressure boundary condition in a multiphase lattice Boltzmann method and its applications on simulations of two-phase flows, Int. J. Numer. Methods Fluids 92 (2020) 669–686, https://doi.org/10.1002/fld.4800.
[37] M.J. Krause, A. Kummerländer, S.J. Avis, H. Kusumaatmaja, D. Dapelo, F. Klemens, et al., OpenLB—open source lattice Boltzmann code, Comput. Math. Appl. 81 (2021) 258–288, https://doi.org/10.1016/j.camwa.2020.04.033.
[38] A. Kummerländer, T. Bingert, F. Bukreev, L.E. Czelusniak, D. Dapelo, C. Gaul, et al., OpenLB Release 1.8.1: Open Source Lattice Boltzmann Code, 2025, https://doi.org/10.5281/ZENODO.15440776.
[39] X. Huang, W. Zhou, D. Deng, Effective diffusion in fibrous porous media: a comparison study between lattice Boltzmann and pore network modeling methods, Materials 14 (2021) 756, https://doi.org/10.3390/ma14040756.
[40] Q. Li, A.J. Wagner, Symmetric free-energy-based multicomponent lattice Boltzmann method, Phys. Rev. E. 76 (2007) 036701, https://doi.org/10.1103/PhysRevE.76.036701.
[41] C. Semprebon, T. Krüger, H. Kusumaatmaja, Ternary free-energy lattice Boltzmann model with tunable surface tensions and contact angles, Phys. Rev. E. 93 (2016) 033305, https://doi.org/10.1103/PhysRevE.93.033305.
[42] X. Shan, H. Chen, Lattice Boltzmann model for simulating flows with multiple phases and components, Phys. Rev. E. 47 (1993) 1815–1819, https://doi.org/10.1103/PhysRevE.47.1815.
[43] A. Xu, Finite-difference lattice-Boltzmann methods for binary fluids, Phys. Rev. E. 71 (2005) 066706, https://doi.org/10.1103/PhysRevE.71.066706.
[44] S.M. Allen, J.W. Cahn, A microscopic theory for antiphase boundary motion and its application to antiphase domain coarsening, Acta Metall. 27 (1979) 1085–1095, https://doi.org/10.1016/0001-6160(79)90196-2.
[45] A. Raeli, E. Salina Borello, C. Serazio, L.E. Czelusniak, T. Bingert, M.J. Krause, Analysis of Lattice Boltzmann Method Potentials for Understanding Underground Fluid Storage Microscale Phenomena. Pap Number OMC-2025-597, 2025.
[46] R. Thirumalaisamy, S. Kim, H. Otomo, J. Jilesen, R. Zhang, Capillary flow simulation with the phase-field-based lattice Boltzmann solver, Phys. Fluids 37 (2025) 022116, https://doi.org/10.1063/5.0249034.
[47] H. Liang, H. Liu, Z. Chai, B. Shi, Lattice Boltzmann method for contact-line motion of binary fluids with high density ratio, Phys. Rev. E. 99 (2019) 063306, https://doi.org/10.1103/PhysRevE.99.063306.
[48] M. Siodlaczek, M. Gaedtke, S. Simonis, M. Schweiker, N. Homma, M.J. Krause, Numerical evaluation of thermal comfort using a large eddy lattice Boltzmann method, Build. Environ. 192 (2021) 107618, https://doi.org/10.1016/j.buildenv.2021.107618.
[49] H. Liang, J. Xu, J. Chen, H. Wang, Z. Chai, B. Shi, Phase-field-based lattice Boltzmann modeling of large-density-ratio two-phase flows, Phys. Rev. E. 97 (2018) 033309, https://doi.org/10.1103/PhysRevE.97.033309.
[50] T. Mitchell, Development of a Multiphase Lattice Boltzmann Model for High-Density and Viscosity Ratio Flows in Unconventional Gas Wells, PhD Thesis., The University of Queensland, 2019, https://doi.org/10.14264/uql.2020.78.
[51] R. Courant, K. Friedrichs, H. Lewy, ber die partiellen Differenzengleichungen der mathematischen Physik, Math. Ann. 100 (1928) 32–74, https://doi.org/10.1007/BF01448839.
[52] I. Ginzburg, D. d'Humières, A. Kuzmin, Optimal stability of advection-diffusion lattice Boltzmann models with two relaxation times for positive/negative equilibrium, J. Stat. Phys. 139 (2010) 1090–1143, https://doi.org/10.1007/s10955-010-9969-9.
[53] M.J. Krause, Fluid flow simulation and optimisation with lattice Boltzmann methods on high performance computers - application to the human respiratory, System (2010), https://doi.org/10.5445/IR/1000019768.
[54] M. Loffredo, C. Serazio, F. Verga, C.F. Pirri, E. Salina Borello, C. Coti, et al., Investigation of pore scale phenomena for underground gas storage through micromodels, in: Offshore Mediterranean Conference and Exhibition, OMC Med Energy Conference and Exhibition, 2025.
[55] A. Olanrewaju, M. Beaugrand, M. Yafia, D. Juncker, Capillary microfluidics in microchannels: from microfluidic networks to capillaric circuits, Lab Chip 18 (2018) 2323–2347, https://doi.org/10.1039/c8lc00458g.
[56] T. Krüger, H. Kusumaatmaja, A. Kuzmin, O. Shardt, G. Silva, E.M. Viggen, The Lattice Boltzmann Method: Principles and Practice, Springer International Publishing, Cham, 2017, https://doi.org/10.1007/978-3-319-44649-3.
[57] S. Succi, The Lattice Boltzmann Equation for Fluid Dynamics and beyond, Oxford University PressOxford, 2001, https://doi.org/10.1093/oso/9780198503989.001.0001.
[58] D. Viberti, C. Peter, E. Salina Borello, F. Panini, Pore structure characterization through path-finding and lattice Boltzmann simulation, Adv. Water Resour. 141 (2020) 103609, https://doi.org/10.1016/j.advwatres.2020.103609.
[59] P. Nathen, D. Gaudlitz, M.J. Krause, N.A. Adams, On the stability and accuracy of the BGK, MRT and RLB Boltzmann schemes for the simulation of turbulent flows, Commun. Comput. Phys. 23 (2018) 846–876, https://doi.org/10.4208/cicp.OA-2016-0229.
[60] S. Simonis, M. Haussmann, L. Kronberg, W. Dörfler, M.J. Krause, Linear and brute force stability of orthogonal moment multiple-relaxation-time lattice Boltzmann methods applied to homogeneous isotropic turbulence, Philos. Trans. R Soc. Math. Phys. Eng. Sci. 379 (2021) 20200405, https://doi.org/10.1098/rsta.2020.0405.
[61] X. Shan, H. Chen, Simulation of nonideal gases and liquid-gas phase transitions by the lattice Boltzmann equation, Phys. Rev. E. 49 (1994) 2941–2948, https://doi.org/10.1103/PhysRevE.49.2941.
[62] S. Zhang, J. Li, R.C.V. Coelho, K. Wu, Q. Zhu, S. Guo, et al., Lattice Boltzmann modeling of forced imbibition dynamics in dual-wetted porous media, Int. J. Multiph. Flow. 182 (2025) 105035, https://doi.org/10.1016/j.ijmultiphaseflow.2024.105035.
[63] Z. Wang, C. Peng, L. Ayala, S. Hosseini, Framework for simulating the partially miscible multi-component hydrocarbon fluids in porous media via the pseudo-potential lattice Boltzmann model, InterPore J. 1 (2024), https://doi.org/10.69631/ipj.v1i1nr7 ipj260424–5.
[64] A.K. Gunstensen, D.H. Rothman, S. Zaleski, G. Zanetti, Lattice Boltzmann model of immiscible fluids, Phys. Rev. A 43 (1991) 4320–4327, https://doi.org/10.1103/PhysRevA.43.4320.
[65] D.H. Rothman, J.M. Keller, Immiscible cellular-automaton fluids, J. Stat. Phys. 52 (1988) 1119–1127, https://doi.org/10.1007/BF01019743.
[66] F. Zahid, J.A. Cunningham, Review of the color gradient lattice Boltzmann method for simulating multi-phase flow in porous media: viscosity, gradient calculation, and fluid acceleration, Fluids 10 (2025) 128, https://doi.org/10.3390/fluids10050128.
[67] M.R. Swift, E. Orlandini, W.R. Osborn, J.M. Yeomans, Lattice Boltzmann simulations of liquid-gas and binary fluid systems, Phys. Rev. E. 54 (1996) 5041–5052, https://doi.org/10.1103/PhysRevE.54.5041.
[68] X. He, S. Chen, R. Zhang, A lattice Boltzmann scheme for incompressible multiphase flow and its application in simulation of Rayleigh–Taylor instability, J. Comput. Phys. 152 (1999) 642–663, https://doi.org/10.1006/jcph.1999.6257.
[69] T. Lee, C.-L. Lin, A stable discretization of the lattice Boltzmann equation for simulation of incompressible two-phase flows at high density ratio, J. Comput. Phys. 206 (2005) 16–47, https://doi.org/10.1016/j.jcp.2004.12.001.
[70] C. Zhao, S. Patel, T. Lee, A difference-free conservative phase-field lattice Boltzmann method, Comput. Fluids 298 (2025) 106674, https://doi.org/10.1016/j.compfluid.2025.106674.
[71] T. Reis, A lattice Boltzmann formulation of the one-fluid model for multiphase flow, J. Comput. Phys. 453 (2022) 110962, https://doi.org/10.1016/j.jcp.2022.110962.
[72] B. Boyd, D. Jarrahbashi, A diffuse-interface method for reducing spurious pressure oscillations in multicomponent transcritical flow simulations, Comput. Fluids 222 (2021) 104924, https://doi.org/10.1016/j.compfluid.2021.104924.
[73] E. Ezzatneshan, A.A. Khosroabadi, On accuracy of lattice Boltzmann method coupled with Cahn-Hilliard and Allen-Cahn equations for simulation of multiphase flows at high-density ratios, J. Appl. Fluid Mech. 15 (2022), https://doi.org/10.47176/jafm.15.06.33536.
[74] K. Wang, Xia Yan-Chen, Z.-Y. Li, A Phase-field Lattice Boltzmann Method for Liquid-Vapor Phase Change Problems Based on Conservative Allen-Cahn Equation and Adaptive Treegrid, 2023.
[75] E. Ezzatneshan, K. Nakhaei, A. Fattahi, Dynamics of particulate droplets collision: an Allen-Cahn based multiphase lattice Boltzmann approach, Comput. Math. Appl. 174 (2024) 167–182, https://doi.org/10.1016/j.camwa.2024.08.029.
[76] Z. Chen, Y.H. Sun, Multiphase lattice Boltzmann flux solver with conservative Allen-Cahn model for modeling high-density-ratio flows, Int. J. Numer. Methods Fluids 96 (2024) 701–718, https://doi.org/10.1002/fld.5265.
[77] S.M. Allen, J.W. Cahn, Mechanisms of phase transformations within the miscibility gap of Fe-rich Fe-Al alloys, Acta Metall. 24 (1976) 425–437, https://doi.org/10.1016/0001-6160(76)90063-8.
[78] Y.H. Qian, D. D'Humières, P. Lallemand, Lattice BGK models for Navier-Stokes equation, Europhys. Lett. EPL 17 (1992) 479–484, https://doi.org/10.1209/0295-5075/17/6/001.
[79] J. Latt, B. Chopard, Lattice Boltzmann method with regularized pre-collision distribution functions, Math. Comput. Simul. 72 (2006) 165–168, https://doi.org/10.1016/j.matcom.2006.05.017.
[80] Q. Zou, X. He, On pressure and velocity boundary conditions for the lattice Boltzmann BGK model, Phys. Fluids 9 (1997) 1591–1598, https://doi.org/10.1063/1.869307.
[81] Q. Lou, Z. Guo, B. Shi, Evaluation of outflow boundary conditions for two-phase lattice Boltzmann equation, Phys. Rev. E. 87 (2013) 063301, https://doi.org/10.1103/PhysRevE.87.063301.
[82] Q.T. Doan, A. Keshavarz, C.R. Miranda, P. Behrenbruch, S. Iglauer, Molecular dynamics simulation of interfacial tension of the CO2-CH4-water and H2-CH4-water systems at the temperature of 300 K and 323 K and pressure up to 70 MPa, J. Energy Storage 66 (2023) 107470, https://doi.org/10.1016/j.est.2023.107470.
[83] L. Hashemi, M. Boon, W. Glerum, R. Farajzadeh, H. Hajibeygi, A comparative study for H 2 –CH 4 mixture wettability in sandstone porous rocks relevant to underground hydrogen storage, Adv. Water Resour. 163 (2022) 104165, https://doi.org/10.1016/j.advwatres.2022.104165.
[84] B. Pan, X. Yin, W. Zhu, Y. Yang, Y. Ju, Y. Yuan, et al., Theoretical study of brine secondary imbibition in sandstone reservoirs: implications for H2, CH4, and CO2 geo-storage, Int. J. Hydrogen Energy 47 (2022) 18058–18066, https://doi.org/10.1016/j.ijhydene.2022.03.275.
[85] R. Lenormand, E. Touboul, C. Zarcone, Numerical models and experiments on immiscible displacements in porous media, J. Fluid Mech. 189 (1988) 165–187, https://doi.org/10.1017/S0022112088000953.
[86] C. Zhang, M. Oostrom, T.W. Wietsma, J.W. Grate, M.G. Warner, Influence of viscous and capillary forces on immiscible fluid displacement: pore-scale experimental study in a water-wet micromodel demonstrating viscous and capillary fingering, Energy Fuel 25 (2011) 3493–3505, https://doi.org/10.1021/ef101732k.